‘Hidden’ HCN channels permit pathway-specific synaptic amplification in L2/3 pyramidal neurons

Viktor János Oláh[1], Jing Wu[2], Leonard K. Kaczmarek[2,3] & Matthew JM Rowan[1,4*]

[1]Department of Cell Biology, Emory University School of Medicine, Atlanta, GA, 30322, USA
[2]Department of Pharmacology, Yale University School of Medicine, New Haven, Connecticut 06520
[3]Department of Cellular and Molecular Physiology, Yale University School of Medicine
[4]Center for Neurodegenerative Disease, Emory University School of Medicine

***Address for Correspondence:**
Matt Rowan, PhD
Emory University School of Medicine
Department of Cell Biology
Atlanta, GA, 30322
Email: mjrowan@emory.edu

Citations: 72; *Figures*: 7 main figures; 4 supplementary figures

ABSTRACT

Layer 2/3 pyramidal cells (L2/3 PCs) play a crucial role in cortical information transfer. Although the dendritic arbors of L2/3 PCs are impressive, they lack the distinct anatomical compartments characteristic of deeper L5 PCs. For example, many L2/3 PCs do not display an apparent distal tuft region. However, L2/3 PCs receive inputs from both thalamic (bottom-up) and cortical (top-down) inputs, preferentially synapsing onto their proximal and distal dendrites, respectively. Nonuniform organization of channels and NMDA receptors in L2/3 dendrites could serve to independently modulate these information streams to affect learning and behavior, yet whether L2/3 PC dendrites possess this capability has not been established. Here, we found a previously unappreciated non-uniform HCN channel distribution in L2/3 PCs, allowing for pathway-specific gating of NMDA receptor recruitment at bottom-up (proximal) but not top-down (distal) synapses. Interestingly, HCN availability could be regulated via neuromodulation, suggesting that the gain of thalamic and cortical-cortical signals in L2/3 may be independently modified in vivo.

INTRODUCTION

Layer 2/3 pyramidal cells (L2/3 PCs) are the most numerous excitatory neuron in the neocortex. As a major component of the canonical circuit, L2/3 PCs are thought to play crucial roles in information transfer and gain control of cortical output(1). Thus, disambiguating the afferent circuit connections of L2/3 PCs has been a significant focus of neuroscience research in the past decade(2-5). However, understanding cellular mechanisms by which L2/3 PCs transform information is equally important (6-9). Like their more extensively studied counterparts (e.g., L5 PCs, hippocampal CA1 PCs), L2/3 PCs are equipped with an array of dendritic nonlinearities(10, 11), enabling complex subcellular computations. Nonetheless, L2/3 PCs exhibit marked disparities from other PC types as well. Their morphology is less segmented, due to the lack of a distinctive apical tuft (except for deep layer 3 cells (12)). Their dendritic protrusions are also shorter, and consequently possess less surface area over which specialized nonlinear operations may be actualized. Therefore, the applicability of currently established neuronal dynamics to L2/3 PCs is questionable.

Dendritic voltage-gated channels and receptors are crucial for diversifying the computational power of neuronal cells, by allowing for nonlinear processing of arriving synaptic inputs(13). Nonlinear processing is essential for proper brain function and has been implicated in critical tasks such as conscious perception(14, 15) and processing of sensory and motor input(16). Therefore, a more comprehensive understanding of subcellular signal processing dynamics in L2/3 PCs is warranted. Dendritic hyperpolarization-activated nonselective cation (HCN) channels are a staple of several PC classes(17, 18), playing essential roles in regulating resting membrane potential, the normalization of synaptic events arriving at spatially mismatched locations, and establishing oscillation frequency-selectivity(19). Beyond exerting control over the general excitability of neurons, HCN channels contribute to synaptic plasticity and regulate working memory(19). In following, HCN dysfunction contributes to mechanisms of epilepsy and pain(20). Electrophysiological detection of this current often relies on identification of a characteristic ‘sag’ potential, elicited by hyperpolarizing current injections. In L2/3 PCs, this sag potential is negligible in most cortical areas (but see (21)) thus, HCN channels are often stated as missing from L2/3 PCs. Therefore, the functional expression of HCN channels in these cells remains ambiguous.

Here we report that L2/3 PCs throughout the cortex express functionally relevant HCN channels with surprising functions. We found that HCN channels robustly influence the overall excitability of L2/3 PCs. Interestingly, we found that HCN channel availability in L2/3 PCs is biased in a unique proximal somato-dendritic manner, which is inverted with respect to L5 and hippocampal CA1 PCs, where HCN is enriched within their distal apical tufts(18, 22). In cooperation with NMDA

receptors, this L2/3 HCN organization could modulate the boosting of proximal 'bottom-up' dendritic inputs, without affecting distal 'top-down' dendritic inputs. Furthermore, we found that HCN expression is robustly upregulated during early postnatal development and that neuromodulation in adulthood can rapidly adjust HCN channel availability. Our results demonstrate that L2/3 PCs not only express dendritic HCN channels, but also employ these conductances in a previously unappreciated manner.

RESULTS

HCN channel expression in L2/3 PCs

HCN channels have been extensively documented and rigorously characterized in several cortical PC types(17), however, whether PCs residing in layer 2/3 of the mouse cortex express functionally relevant HCN channels remains ambiguous. Nonetheless, open-source snRNAseq (23) shows comparable HCN subunit mRNA levels in all cortical PC types of the visual cortex (Fig. 1a). Therefore, we investigated whether this mRNA signature translated to HCN surface expression. Immunohistochemical staining against HCN1 showed discernible somatic fluorescent signal in many cells residing in superficial layers of the cortex (Fig. 1b) along with staining of putative dendrites. To examine the potential functional role for HCN channels in L2/3 PCs, we performed *ex vivo* cell-attached recordings from visually identified L2/3 PCs in the primary visual cortex from mature mice. Spike output upon extracellular stimulation (50 Hz) in layer 4 was then measured in control conditions and following pharmacological HCN channel block (Fig. 1c). We found that bath application of Cs^+ (1mM), a conventional blocker of HCN channels at this concentration, significantly increased their firing (Fig. 1d). This was unlikely due to presynaptic modulation of these synapses, as the paired-pulse ratio was unchanged in a set of separate whole cell recordings coupled with stimulation in layer 4 (Fig. 1e). Together, these results suggest that L2/3 PCs express a functionally relevant set of HCN channels which are essential for limiting excess AP firing following synaptic stimulation.

HCN channels constrain the overall excitability of L2/3 PCs

To investigate the role of HCN channels in regulating the excitability of L2/3 PCs, we next performed further L2/3 PC whole-cell recordings. A conventionally used assessment of HCN channel function is the characterization of the sag potential(17). This hallmark of I_h activation is measured as the amount

of rectification detected in response to hyperpolarizing current injections. In line with previous reports, we found that L2/3 PCs exhibited an unremarkable amount of sag potential at 'typical' current commands. However, upon larger negative current injections, a discernable rectification was revealed (Fig. 2a). In addition, the rectification of the steady-state responses was abolished in the presence of external Cs^+ which could be restored by artificial I_h supplementation by dynamic clamp (Fig. 2b). Similarly, sag was non-detectable when I_h was blocked, which could then be restored by dynamic clamp (Fig. 2c,d). Furthermore, we found that passive electrical properties were also significantly modulated by HCN blockade (Fig. 2e,f). Together these results explain the dramatic effect of Cs^+ on excitability (Fig. 1). The non-apparent sag potential at conventional hyperpolarizing current steps is thus surprising, suggesting a markedly faster occurrence of the I_h effect exists in L2/3 PCs which occludes the biphasic nature of the sag response. To investigate this possibility, we measured the time-constant of the immediate voltage responses. We found a strong positive correlation between the amplitude of a passive current command and the voltage response time constant, which was abolished by Cs^+ bath application (Fig. 2g). This confirms that I_h has a strong effect during the initial phase of hyperpolarizing voltage responses which may contribute to the lack of detectable sag potential at modest current injections. However, other biophysical mechanisms may also contribute to the muted sag effect in L2/3 PCs.

Next, we examined the voltage dependence and kinetic properties of I_h in L2/3 PCs in voltage clamp (Fig. 2h). Significant Cs^+-sensitive (1mM) currents were activated at subthreshold membrane potentials, with half-activation voltages more negative than the resting membrane potential, and with relatively fast activation kinetics (Fig. 2i,j). Overall the pharmacological profile, effects on passive electrical properties, and voltage dependence all point to previously published data describing HCN channels (24). Together these results indicate that L2/3 PCs express a functionally relevant population of HCN channels, which constrain the excitability of these cells. Similar voltage clamp responses were observed beyond the visual cortex (e.g., in S1, M1, and A1; Supplementary Fig. 1) suggesting that HCN channels are a consistent feature in L2/3 PCs across sensory cortices.

Noncanonical subthreshold signal processing in L2/3 PCs by I_h

Electrical signals at different dendritic compartments undergo distance-dependent distortion (22, 25), which has a major effect on neuronal function in cells with extensive dendritic branching (26). To counteract these effects, larger L5 PCs and CA1 PCs express HCN channels with nonuniform

distributions (18, 24). As L2/3 PCs have a much more compact morphology, synaptic input distortions might be less severe, raising the possibility of an alternative function of HCN channels in these cells. Thus, to investigate the distance-dependence of HCN on L2/3 synaptic inputs we made whole-cell patch recordings from Alexa-594 filled L2/3 PCs, and performed extracellular minimal stimulation at different dendritic locations guided with 2P microscopy (Fig. 3a). Elicited EPSPs likely reflect the activation of a single axon as stimulus intensity was set to achieve an ~50% failure rate(27). As HCN deactivation has been shown to strongly impact the duration of synaptic events(22, 25), we quantified changes in the half-width of locally evoked EPSPs, here using the HCN-selective blocker ZD-7288 (50 μM). Surprisingly, our results were in contrast to previous reports in L5 and CA1 PCs, in that I_h block had a far smaller effect on the time-course of distally-evoked (>100 μm distance from the soma) synaptic responses. In contrast, proximal inputs (<100 μm) were markedly more broadened after I_h blockade (Fig. 3b,c). These results suggest that L2/3 PCs are equipped with a distinctive subcellular HCN distribution, potentially contributing to noncanonical distance-dependent input modulation along the dendritic axis of L2/3 cells.

Pathway-specific modulation of synaptic information

L2/3 PCs receive information from distinct brain regions, such as "top-down" (cortical-cortical) axons, generally arriving to layer 1(28) and "bottom-up" (thalamocortical/layer 4) axons, terminating on proximal dendrites located in layer 4 and 2/3(29). Due to the stronger proximal effect of HCN on L2/3 PC EPSPs, we explored whether this modulation yielded input-pathway-specific differences. Whole-cell recordings were again obtained from L2/3 PCs, and EPSPs were elicited by minimal stimulation with electrodes situated to preferentially stimulate either layer 4 or layer 1 axons (electrode placement ~200μm laterally from recorded PC in either layer). In a subset of our recordings stimulating layer 4 inputs, evoked EPSPs were substantially larger than spontaneously occurring events (Fig. 3d). We deemed these as inputs arriving directly from the lateral geniculate nucleus axons (putative direct thalamocortical input(30) from the LGN, Supplementary Figure 2.). I_h blockade significantly broadened elicited EPSPs when the stimulation electrode was placed in layer 4, but not in layer 1 (Fig. 3e). Consequently, the voltage integral of EPSPs was significantly larger for L4 inputs compared to those in L1 (Fig. 3f). The effect of Cs^+ on EPSP half-width and voltage integral was similar for both L4 and putative LGN inputs, suggesting intermingled termination zones(29). Together these results

suggest that HCN channels preferentially regulate bottom-up nonlinear signaling in proximal dendritic regions in L2/3 PCs.

HCN channels are notable for their ability to restrain temporal integration of synaptic inputs(22). Therefore, we repeated these experiments using more high-frequency stimulation (5 stimuli at 50 Hz; Fig. 3g). In accordance with the effect on single EPSPs, summation of L1 (i.e., 'distal) inputs was unaltered with HCN block. In contrast, HCN blockade led to increased temporal summation of L4 inputs (Fig. 3h,i). However, summation of putative LGN inputs was not affected by HCN channel block, suggesting further diversification of active properties even between L4 and LGN inputs as well.

I_h channels constrain NMDA receptor-dependent synaptic boosting

In a passive environment, dendritic filtering (31) creates attenuated (i.e., wider) EPSPs when originating further from the soma. Yet our results show an opposite phenomenon with HCN channels blocked. It has been described that reduced HCN availability can facilitate dendritic boosting mechanisms, via activation of either voltage-gated (32) or NDMA (33) channels. To investigate possible contributions of dendritic voltage-dependent processes, we performed NEURON computational simulations using a realistic L2/3 PC dendritic morphology (34). Inserting voltage-gated sodium or potassium channels with various distributions could not recapitulate our distance-dependent EPSP observations (Supplementary Figure 3.). Thus, we next investigated whether NMDA receptors might play a role in the observed phenomenon, due to their described overwhelming contribution to *in vivo* activity in L2/3 PCs (8, 35).

We first tested whether NMDA receptors contribute to spontaneously occurring synaptic inputs (sEPSPs) in L2/3 PCs(36). Due to potential alterations in spontaneous release and overall circuit activity, extracellularly applied NMDA blockers may introduce significant confounds for this line of investigation, especially as spontaneous synaptic potentials show tremendous variability in frequency, amplitude, and kinetics. To overcome this conundrum, we designed a custom-built pipette attachment through which the intracellular solution could be stably exchanged during whole-cell recordings (37). We recorded sEPSPs in L2/3 PCs first using control intracellular solution, which was then exchanged to a 50 µM MK-801 (non-competitive NMDA receptor antagonist) containing intracellular solution (Fig. 4a). To also capitalize on the voltage-sensitivity of NMDA receptors, average peak amplitudes were recorded at two different membrane potentials for each intracellular condition; -80 mV and -55

mV (resting membrane potential, and a somatic membrane potential depolarized enough to partially unblock NMDA receptors (38)). Due to the small nature of sEPSPs, quantification of other waveform parameters (i.e., EPSP width) was avoided. After quantifying the mean sEPSP peak at -80 mV, we calculated the expected (linear) sEPSP peak at -55 mV and compared this prediction to our observations of -55 mV. We found that sEPSPs were significantly larger than predicted after depolarization (Fig. 4b), alluding to the presence of a nonlinear boosting mechanism. We found that intracellular MK-801 solution exchange could abolish this synaptic amplification (Fig. 4c), indicating that NMDA receptors actively contribute to shaping naturally occurring sEPSPs in L2/3 PCs. The effect of pipette perfusion itself on our measurements was negligible (Supplementary Figure 4)

Having established that NMDA receptors play an active role in modulating sEPSPs, we next explored whether differential NMDA recruitment could explain the observed boosting of proximal synaptic inputs following HCN blockade described earlier. Computational simulations (lacking HCN) (Fig. 4d) revealed that a proximally-biased NMDA distribution, as seen in other PC types (39), could indeed recapitulate our experimental findings in L2/3 PCs with high accuracy (Fig. 4e,f). Because HCN channels can reduce NMDA recruitment during synaptic signaling, we next explored whether proximal enrichment of HCN allows for bottom-up-specific gating of NMDA (Fig. 4g). To accomplish this, we recorded L2/3 EPSPs following stimulation of both proximal L4 and distal L1 inputs, as described earlier, during each recording and varied the background pharmacology. Intriguingly, L4-evoked EPSPs were slightly narrower than L1 in control conditions, potentially owing to increased HCN in proximal dendrites. This layer-specific relationship was inverted following extracellular Cs^+ to block HCN (Fig. 4g,h). To confirm that this L4-specific EPSP broadening after HCN channel block was due to NMDA-inducted boosting, as predicted in our simulations (Fig. 4f), we next examined the EPSPs with Cs^+ and MK-801 together. In the presence of internal MK-801, the broadening effect of Cs^+ on L4-evoked EPSPs was abolished, thereby reverting the L4-L1 EPSP relationship to a control-like state. (Fig. 4g,h). Together, our modelling and experimental results indicate that NMDA-directed amplification of L4 inputs is strongly constrained by a proximal HCN bias in L2/3 PCs dendrites, allowing for pathway-specific modulation of ‘bottom-up’ inputs without affecting those arriving from ‘top-down’ L1 axons.

Noncanonical HCN distribution predicted in L2/3 PCs

We next carried out computational simulations for HCN in L2/3 PCs, based on our previous observations and modeling. To reproduce the native relationship between EPSP halfwidth and dendritic distance, HCN channels were inserted into the model with different distributions and conductance densities (Fig 5a). Our simulations revealed that proximal bias in HCN channel distributions could best recapitulate our observations of HCN on proximally and distally originating EPSP halfwidths. providing the best fit to our measurements (Fig. 5b,c). According to these simulations, HCN regulation of local input resistance constrained voltage-dependent NMDA receptor activation. This is in line with the proximal HCN1 channel staining (Fig. 1) revealed by immunohistochemistry. These results suggest that L2/3 PCs have a unique proximal HCN channel bias, as previous experiments show a distal HCN expression in L5 PCs and CA1 PCs(18, 24). Possibly due to the markedly different morphology, specifically the absence of an independent computational tuft unit, HCN channels have different functions in L2/3 PCs. Thus, together with experimental observations, these simulations indicate that HCN channels are well positioned to regulate bottom-up proximal inputs in L2/3 PCs, contrary to their L5 PC counterparts, which express HCN distally to counteract distance dependent passive filtering from top-down inputs.

Tight developmental upregulation of Layer 2/3 HCN channels

Several ion channels show postnatal maturation in their biophysical properties and surface expression(40), raising the possibility of a different proximo-distal HCN bias in young L2/3 PCs compared to adult animals. To examine this possibility, L2/3 PCs were recorded at three developmental time points (1st, 2nd and 6th postnatal week) in S1. Our initial assessment of HCN maturation showed that a rapid developmental upregulation occurs between 1 and 2 weeks old. We opted to perform further developmental experiments in primary somatosensory cortex, where cells already receive adequate bottom-up information during the first and second postnatal week.

We found that 1 week old L2/3 PCs displayed markedly different passive properties, while 2-week-old cells were quite similar to mature cells (Fig. 6a). The non-quantifiable sag potential in 1 week old animals implies the lack of I_h current at this developmental time point, however, the disproportionately large input resistance and elevated resting membrane potential also suggests that other background leak channels may also be missing at this developmental window (Fig. 6b). Subsequent voltage clamp recordings confirmed that L2/3 PCs in 1 week old animals do not possess a considerable amount of I_h in contrast to 2 and 6 week old animals (Fig. 6c,d). We found that both resting membrane potential and

peak I_h conductance changes throughout development were tightly (negatively) correlated (Fig. 6e). This provides additional evidence for parallel maturation of HCN with other leaky channels, as HCN channel expression alone would be predicted to shift the membrane to more depolarized potentials (Fig. 2e). Next, we mapped the distance-dependence dendritic EPSP kinetics in 1 week old animals (Fig. 6f). We found a surprising 'non-Rall-ian' negative correlation between EPSP halfwidth and stimulation distance from the soma (Fig. 6g, h), similar to our previous results from mature neurons with HCN channels blocked (Fig. 3a,b). This suggests the presence of nonlinear boosting mechanisms in proximal dendrites of developing L2/3 PCs, similar to mature cells, which are unabated due to the lack of HCN at this developmental stage.

I_h dependent neuromodulation of L2/3 PC activity by serotonergic inputs

If the robust dendritic HCN availability in mature L2/3 PCs is unalterable, the ability of NMDA to modulate bottom-up inputs might be inadequate. Whether the mature brain possesses mechanisms to modulate HCN in L2/3 PCs is unknown. Nonetheless, previous work in cortical L5 PCs shows that I_h currents can be modulated following 5-HT_7 serotonergic receptor activation(41). L2/3 PCs are extensively innervated by serotonergic axons from the dorsal raphe (42), providing a potential framework to modify HCN availability. Single-cell RNA-seq (23) showed that L2/3 PCs do express 5-HT_7 receptors, interestingly at higher levels than all other cortical PCs (Fig. 7a). We pharmacologically evaluated a potential role of serotonergic HCN regulation by bath application of 5-carboxamidotryptamine (5-CT; 30 nM), a specific 5-HT_7 agonist. 5-CT application significantly reduced evoked firing of L2/3 PCs during extracellular stimulation in L4 (Fig. 7b). Voltage clamp experiments revealed that the rectification of steady-state voltage responses to hyperpolarizing current injection was amplified with 5-CT (Fig. 7c), likely due to the increased availability of HCN channels due to a rightward shift in their activation voltage-dependence (Fig. 7d). 5-CT also reduced L2/3 input resistance potentially via HCN regulation, however, did not yield a depolarizing effect on the resting membrane potential nor affect AP threshold (Fig. 7e). Importantly, 5-CT had no impact on the firing responses of L2/3 PCs when I_h currents were blocked with background Cs^+ throughout the experiment (Fig. 7f). Furthermore, the dampening of neuronal output was not related to an downregulating effect of 5-HT7 on NMDA receptors (Fig. 7g, (43)). Together these results indicate that neuromodulation represents an endogenous mechanism by which HCN availability can be altered in L2/3 PCs.

DISCUSSION

Precise communication between cortical neurons relies on discrete pre- and postsynaptic forms of information transfer at synapses. The majority of cortical synapses terminate along the dendritic tree (44) where, based on local active and passive electrical properties, various types of nonlinear transformations occur. The spatially and electrically disjointed nature of dendrites (45) from the rest of the cell allows for local, soma-independent computation. For example, perturbing active dendritic elements (i.e., local conductances) can impair several fundamental cortical circuit tasks (36) such as perception (14), underlining the necessity for compartmentalized information processing. Further, single-subunit model simulations are unable to reproduce *in vivo* observed activity patterns of L2/3 PCs(9). Here, by combining *ex vivo* current clamp, synaptic stimulation, and ion channel recordings with empirically informed, biophysically realistic simulations, we demonstrate that L2/3 PCs in sensory cortex express a previously unappreciated, proximally-biased HCN channel distribution. Due to an apparent universal HCN expression in L2/3 cells from each region, this arrangement should allow for modification of synaptic gain across all primary sensory areas of cortex. One of the basic functions of L2/3 PCs in sensory cortex is to encode first-order information, such as the orientation of visual input(2, 46, 47). Several investigations propose that arithmetic summation of a number of similarly tuned synapses will dictate whether these neurons will fire in response to sensory input (48). However, numerous dendritic nonlinearities have been established in L2/3 PCs, such as NMDA receptors (8) sodium channels (11) and calcium channels (10, 49) which also contribute to this process. Here we demonstrate that L2/3 PCs express a functionally relevant population of HCN channels well situated to modify the gain of cortical sensory and contextual information processing.

We found that HCN channels in L2/3 could constrain fundamental aspects of cellular excitability, such as input resistance and resting membrane potential. This is likely due to a strong proximal somato-dendritic distribution of HCN channels, as observed in immunohistochemical experiments here. Likely due to their influence on input resistance, HCN blockade resulted in greatly increased AP firing during extracellular stimulation. L2/3 HCN channels strongly dampened excitatory synaptic inputs, however, only to those arriving at proximal dendritic locations. In line with this result, HCN channels reduced the timecourse of synaptic inputs following local stimulation in L4, but left those following L1 stimulation unaffected. Together with additional input-specific pharmacological experiments, NEURON simulations demonstrated that this input-specific synaptic phenomenon could indeed be explained by a proximal HCN channel distribution in dendrites putatively situated in L4 and L2/3. This was apparently only possible with a concurrent proximal NMDA recruitment bias. This

should not be confused with observed differences in NMDA recruitment along the axis of individual L2/3 basal dendrites (36). Although a proximal-basal dendrite NMDA receptor distribution is in line with findings from L5 PCs (50), HCN channels are instead enriched distal dendritic compartments in these PC types (18, 24). Thus the unprecedented proximal HCN recruitment in L2/3 PCs permits pathway-specific control of synaptic amplification, as bottom-up (i.e., L4 originating) inputs target proximal dendritic compartments homogeneously (29). This was in opposition to top-down inputs, whose axons largely target distal dendrites in L2/3 PCs (28, 51), as these synapses were unaffected by HCN channel blockade. To fully understand how compartment-specific pathways are functionally regulated, further anatomical and *in vivo* imaging experiments are needed to establish the distribution and synaptic dynamics of L4 and L1 inputs along the L2/3 PC dendritic tree.

HCN channels appear well suited to regulate the synaptic and intrinsic properties of L2/3 PCs, for example, if their availability is plastic or developmentally regulated. Previously, we found that HCN channel availability was upregulated in GABAergic interneurons during development, resulting in reduced propagation of subthreshold signals in mature axons (52). Interestingly, we found that L2/3 PCs in young animals (1 week old) lacked HCN channels. Together, these results suggest a universal, cell-nonautonomous developmental HCN upregulation in both dendritic and axonal compartments. In L2/3 PCs, the HCN channel maturation window was rapid and almost complete by the second postnatal week. Therefore critical period plasticity (53) and developmental I_h upregulation occur during a similar developmental window, suggesting a causal relationship. In addition to the robust developmental regulation of HCN channels, we also found that enhancement of HCN channel availability was also possible in the adult cortex, following serotonergic (5-HT_7) receptor-mediated biophysical regulation. This was likely due to a metabotropic process that increases cytosolic cAMP levels by stimulating adenylate cyclase(54) which in turn modulates HCN channel properties. This raises the intriguing possibility that neuromodulation could induce nonstationary conditions in mature L2/3 circuits, for example, in re-biasing of bottom-up vs. top-down information, experience-dependent plasticity (55), or even for reopening of critical window-like states (56).

As L2/3 PCs are one of the most abundant cell populations of the neocortex, HCN channels in these cells may exert overwhelming control over cortical excitability and thus cognition and memory. Cell non-autonomous HCN channel dysregulation manifests in clear behavioral changes, such as altered spatial learning (57) or impaired working memory (58). Curiously, higher HCN1 protein levels in the postmortem brain also correlate with cognitive resilience in aging humans (59). Therapeutic HCN channel modulation aimed at restoring healthy brain function in distinct pathophysiological states has consequently garnered significant interest (60-62) as both HCN1 and HCN2 are linked to

neuropathic pain (63) and for treating major depressive disorder (61, 62, 64). Here we demonstrate that activation of the serotonergic receptor 5-HT_7 alters HCN channel function in L2/3 PCs, resulting in reduced PC excitability, similar to L5 PCs (41). 5-HT_7 receptor targeting agents are highly effective psychopharmacological compounds. Agents such as the antidepressant *vortioxetine* has a relevant therapeutic concentration that functionally suppresses 5-HT_7 (65), and the mood-stabilizing antipsychotic agent *lurasidone* possesses an even higher binding affinity to 5-HT_7 (66). Commonly used anesthetic drugs also modulate HCN channel action (67, 68), implying the need to investigate anesthesia-related mechanisms and confounds in L2/3 in both therapeutic and experimental settings. Together, we argue that HCN channels are present and functionally relevant in L2/3 PCs. As L2/3 PCs are one of the largest cell populations in the brain, and as HCN channels are the target of several current therapeutics, future research should consider their role in these cells in basic and clinical studies.

METHODS

Acute slice preparation

All animal procedures were approved by the Emory University IACUC. Acute slices from cortex were prepared from mature C57Bl/6J mice (6–10 weeks old). Male and female mice were used for all experiments with data collected from ≥3 mice per experimental condition. Mice were first anesthetized and perfused with ice-cold cutting solution (in mM) 87 NaCl, 25 $NaHO_3$, 2.5 KCl, 1.25 NaH_2PO_4, 7 $MgCl_2$, 0.5 $CaCl_2$, 10 glucose, and 7 sucrose. Thereafter, mice were terminated by decapitation and the brain immediately removed by dissection. Brain slices (250 μm) were sectioned in the coronal plane using a vibrating blade microtome (VT1200S, Leica Biosystems) in the same solution. Slices were transferred to an incubation chamber and maintained at 34°C for ~30 min and then at 23–24°C thereafter. During whole-cell recordings, slices were continuously perfused with (in mM) 128 NaCl, 26.2 $NaHO_3$, 2.5 KCl, 1 NaH_2PO_4, 1.5 $CaCl_2$, 1.5$MgCl_2$, and 11 glucose, maintained at 30.0°C ± 0.5°C. All solutions were equilibrated and maintained with carbogen gas (95% O_2/5% CO_2) throughout.

Electrophysiology

L2/3 PCs neurons were targeted for somatic whole-cell recording in the layer 2/3 region of primary visual cortex by gradient-contrast video microscopy. Electrophysiological recordings were obtained using Multiclamp 700B amplifiers (Molecular Devices). Signals were filtered at 6–10 kHz and sampled

at 50 kHz with the Digidata 1440B digitizer (Molecular Devices). For whole-cell recordings, borosilicate patch pipettes were filled with an intracellular solution containing (in mM) 124 potassium gluconate, 2 KCl, 9 HEPES, 4 $MgCl_2$, 4 NaATP, 3 l-ascorbic acid, and 0.5 NaGTP. Pipette capacitance was neutralized in all recordings and electrode series resistance compensated using bridge balance in current clamp. Liquid junction potentials were uncorrected.

For cell attached recordings seal resistance of >1GΩ was established, for accurate measurement of action potentials. A stimulating electrode was placed in either layer 4 or layer 1 region of the visual cortex, at least 200 µm away from the recorded soma. Stimulation intensities were calibrated to reliably elicit at least 3, but no more than 10 action potentials during the 20 consequent stimuli (50 Hz, 30 s inter-trace intervals, 10-50 µs stimulus length). Stability of the elicited responses was confirmed by an initial 15 repeated measurements. Recordings were post hoc filtered at 2 kHz to remove stimulation artifacts.

Recordings had a series resistance <20 MΩ. Membrane potentials maintained near –80 mV during current-clamp recordings using constant current bias. AP trains were initiated by somatic current injection (300 ms) normalized to the cellular capacitance in each recording measured immediately in voltage clamp after breakthrough (69). Cellular electrical and firing parameters were established by recording voltage responses to current steps between-6 pA/pF and 20 pA/pF. Input resistance was measured by averaging voltage responses to a 20 pA prepulse current step. Sag ratio was determined as the ratio between the sag amplitude and the steady-state response during increasing -2 pA/pF current steps.

To establish distance dependent EPSP kinetics, cells were filled with 10 µM Alexa-594. Dendrites were visualized after cell fill with Alexa 594 (30µM) with two-photon laser scanning microscopy using a commercial scan head (Ultima; Bruker Corp) fitted with galvanometer mirrors using a 60x, 1.0 NA objective. The fluorophore was allowed to equilibrate for at least 10 minutes before imaging. The stimulating electrode, filled with extracellular recording solution, was placed in close proximity (<5 µm) of the two-photon visualized dendrite. Stimulation intensity was calibrated to elicit an EPSP with <1 ms delay and approximately 50% failure rate (54.21 ± 8.72%, n= 41). The 50% failure rate was necessary in order to maximize the possibility of stimulating a single input. For layer 1, layer 4, and putative LGN input stimulations the procedure was the same. Synaptic summation was probed by eliciting 5 consequent responses at 50 Hz. Stimulation intensity was elevated during these recordings

to elicit synaptic responses every time for the first stimuli as failures introduced by lower stimulation intensities can yield inconsistent input activation during the 5 stimuli.

For voltage-clamp recordings, cells were patched in normal extracellular solution to first record their firing patterns. Voltage protocols for I_h current measurements consisted of 300 or 500 ms long voltage steps between −150 and −60 mV. Activation time constant was measured by fitting the initial 100 ms of the current response with a single exponential function. In a subset of recordings CsMeSO4 (2 mM) was bath applied after recording control current responses, to establish cesium-sensitive I_h current kinetics and voltage dependence by subtraction. Series resistances were between 6–20 MΩ (75–80% compensated with 53 µs lag) and were constantly monitored. Data were discarded if the series resistance changed more than 25%.

The dynamic clamp system was built in-house based on a previous publication(70), related online available materials (http://www.dynamicclamp.com/). The equations governing the implemented gHCN were identical to those used in the NEURON model construction. Synaptic conductances were built-in predefined conductances available from http://www.dynamicclamp.com/.

Intracellular solution perfusion

Intracellular solution was perfused by a custom-built tubing and relay system attached to the pipette holder. Briefly, the pipette was filled with normal intracellular solutions to measure firing patterns and subsequent control measurements of spontaneous and elicited EPSPs. Next, a second intracellular solution was introduced to the pipette through a small tube drilled through the pipette holder, by applying miniscule positive pressure. The intracellular fluid levels were marked before the recording and through a second tube the intracellular solution was siphoned out, to not alter established pipette capacitance. During initial trial experiments using fluorophores in the second intracellular solution it was determined that two minutes is enough for complete exchange of the intracellular solution and intracellular equilibration as well. Data were discarded if the series resistance or pipette capacitance changed more than 20%.

Immunohistochemistry

Two-month-old mice were anesthetized with Nembutal (50mg/mL, i.p.) and perfused transcardially with 4% paraformaldehyde (PFA), 0.05% glutaraldehyde in phosphate buffered saline (PBS). After

perfusion, brains were removed from the skull and immersed in 4% PFA overnight at 4°C. Coronal 100 µm-thick sections were then cut on a Vibratome (Leica V1000). Brain slices were permeabilized and incubated in blocking buffer for one hour at room temperature. After blocking, sections were overlaid with primary antibody to HCN1 (1:200, Thermo Fisher Scientific) overnight at 4 °C, then subjected to a 1 h incubation with secondary antibody (Goat anti-Rabbit IgG, 1:200, Thermo Fisher Scientific) at room temperature. Stained sections were mounted with DAPI-containing mounting solution and sealed with glass coverslips. Confocal imaging was carried out on a Leica SP5 MP.

PV cell NEURON modeling

Computer simulations were performed using the NEURON simulation environment (versions 7.5 and 7.6, downloaded from http://neuron.yale.edu). A constrained NEURON model with an active somatic compartment was downloaded from the publicly available Cell Type Database of the Allen Institute (http://celltypes.brain-map.org/experiment/electrophysiology/487661754). Passive properties (axial resistance, specific membrane capacitance and leak conductance density) were altered to recreate passive membrane potential responses of whole-cell recorded L2/3 PCs for given stimulus intensities. Both transient and persistent potassium channels were taken out of the model to gain simulation speed as the aim of the simulations was to reproduce subthreshold EPSP dynamics. Final simulations were rerun with intact sodium currents as well to confirm the lack of alterations introduced by these channels. The I_h conductance was based on the built-in Hodgkin–Huxley model of NEURON with freely adjustable sets of parameters(71). I_h model parameters were constrained by our whole-cell voltage clamp recordings. The steady-state activation was governed by the following equation:

$$minf = \frac{1}{1 + e^{\frac{v+21.945}{6.85}}}$$

where v is the local membrane potential. Due to the lack of apparent inactivation, the model operated with a single gate (activation).

The activation and deactivation time constant was defined as

$$mtau = 25.46 * e^{-0.5*\left(\frac{v+100.28}{16.2}\right)^2}$$

To simulate EPSP kinetics, a movable spine (length: 0.6 µm, diameter: 0.6 µm, axial resistance: 150 Ωcm), with spine neck (length: 2 µm, diameter: 0.1 µm, axial resistance: 100 Ωcm) was created. Leak conductance was inserted into both compartments, along with the fitted conductance model. Synaptic inputs were supplemented by using NEURON's built-in AlphaSynapse class. To probe the contribution of specific dendritic conductances to shaping the distance-EPSP halfwidth relationship, selected conductance models were inserted into both apical and basal dendrites with a Gaussian distribution. This curve was selected as modulation of the Gaussian curve's width and y-offset can reproduce a wide variety of feasible distributions such as linear, exponential, or hot-zone-like expression. To model the contribution of dendritic sodium, potassium, and calcium channels to input modulation, NaTs, Kv3_1 and Ca_LVA models were selected. Distribution approximation was done by grid search to avoid local fitting minimums. NMDA receptors were implemented based on a previous publication (72). During the fitting procedure, NDMA activation voltage and AMPA:NMDA ratios were adjusted.

Statistics

Averages of multiple measurements are presented as mean ± SD. Data were statistically analyzed by ANOVA test using Origin software and custom-written Python scripts. Normality of the data was analyzed with Shapira-Wilks test.

Data and software availability

All code used for simulating single and multicompartmental NEURON models will be made available on Github and public repositories.

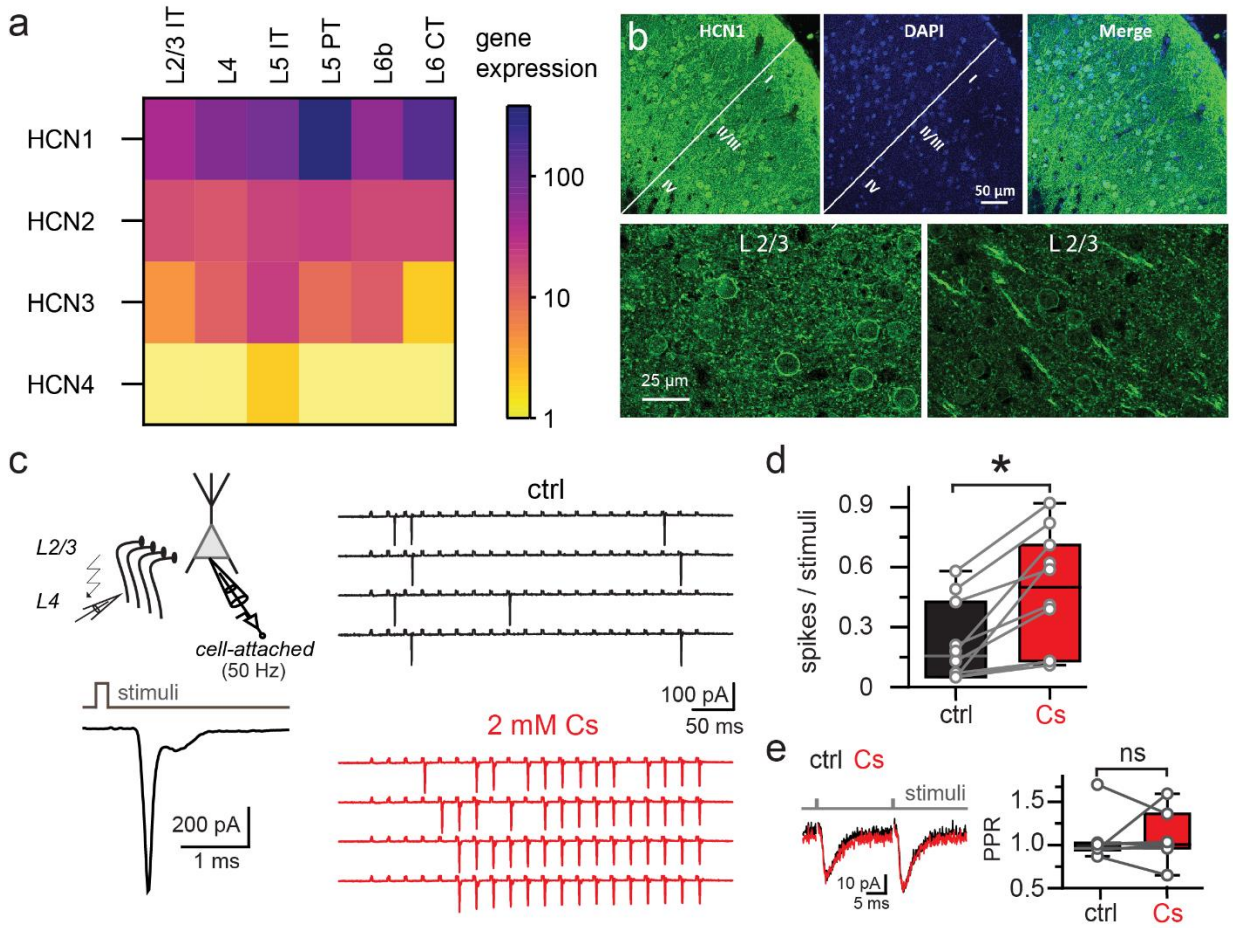

Fig 1. Abundant HCN expression in cortical L2/3 PCs

a. HCN gene subunits show uniform expression pattern among cortical PC types. Data is collected from the online available dataset(23). **b.** HCN1 immunohistochemistry reveals dense somatic expression in layer 2/3 of the visual cortex **c.** HCN channels control the excitability of L2/3 PCs. Schematic illustration of the experimental arrangement of cell attached recordings during extracellular stimulation of L4, and the shape of the elicited action potential (left). Increased spiking of L2/3 PC upon blockade of HCN channels with 2 mM CsMeSO4 (right). **d.** Pharmacological block of I_h significantly increases the firing response of L2/3 PCs (0.22 ± 0.06 Hz vs. 0.48 ± 0.09 Hz for control vs CsMeSO4 bath application, p=0.002, t(9)=-4.42, Student's paired t-test, n=10. **e.** Presynaptic contributions were examined using the paired-pulse ratio (PPR) in whole cell current clamp recordings (1.09 ± 0.12 Hz vs. 1.17 ± 0.15 Hz for control vs CsMeSO4 bath application, p=0.422, t(6)=-0.8612, Student's paired t-test, n=7).

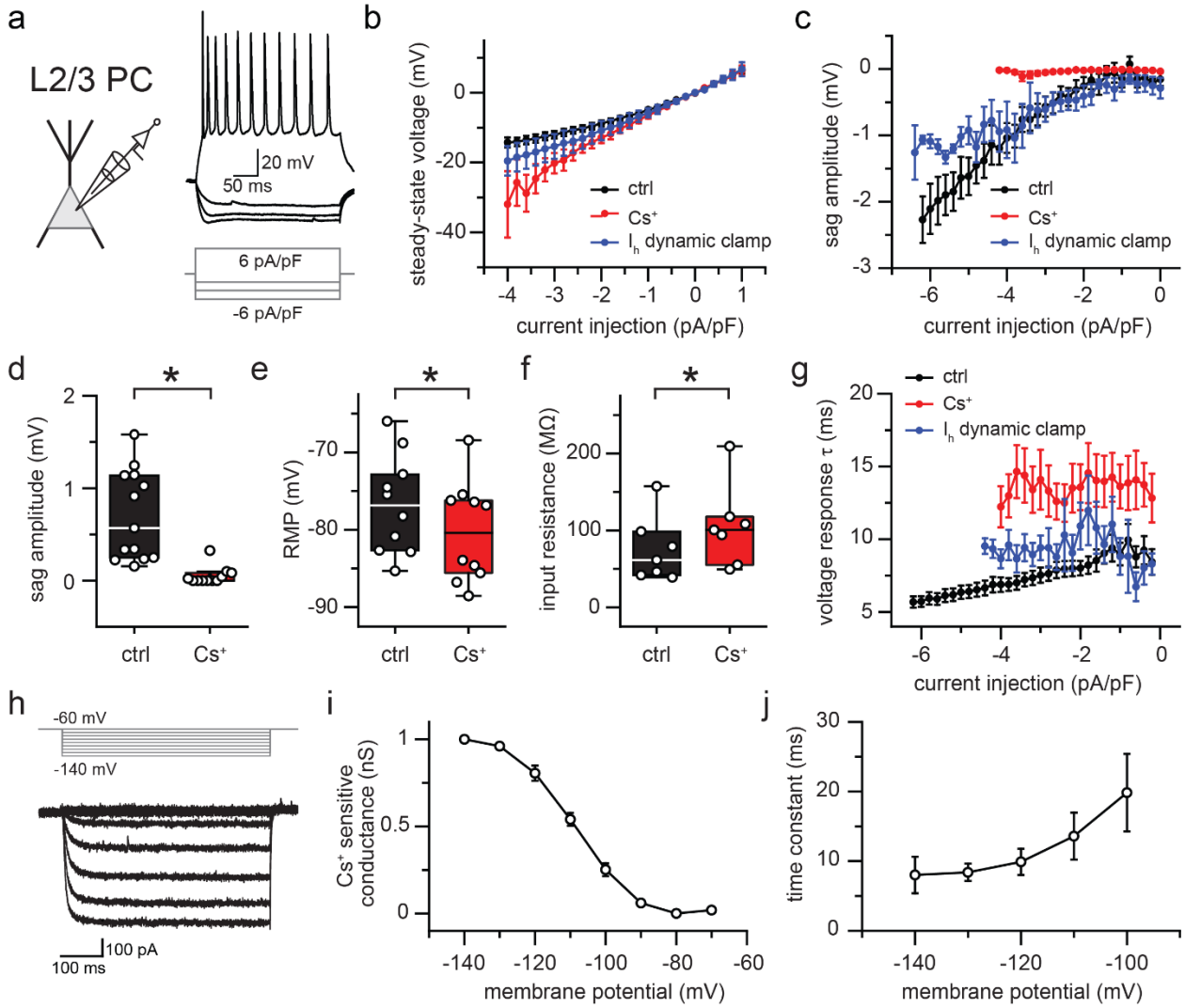

Fig 2. Functionally relevant I_h in L2/3 PCs

a. Whole cell current clamp recordings showing sag response to very negative current commands. **b.** Steady-state voltage response rectification upon hyperpolarizing current injections is mediated by I_h. **c.** Sag voltage is abolished by blocking I_h. **d.** Sag amplitude is Cs^+ sensitive (0.7 ± 0.49 mV vs. 0.05 ± 0.1 mV for control vs CsMeSO4 application, $p=2.46^{-4}$, t(22)=4.37, Student's two-sample t-test, n=13 and 11). **e.** Resting membrane potential is modulated by I_h (-76.75 ± 6.37 mV vs. -80.29 ± 6.48 mV for control vs CsMeSO4 bath application, $p=1.98^{-4}$, t(9)=6.02, Student's paired t-test, n=10). **f.** Input resistance is altered by I_h (74.78 ± 42.34 mV vs. 104.99 ± 52.91 mV for control vs CsMeSO4 bath application, p=0.048, t(6)=-2.48, Student's paired t-test, n=7). **g.** The time course of voltage responses to hyperpolarizing current on the magnitude of the current injection is abolished by Cs^+. **h.** Example voltage clamp recording of cesium sensitive currents in a L2/3 PC. **I.** Voltage dependence of cesium sensitive current activation, **J.** Voltage dependent activation kinetics of cesium sensitive currents.

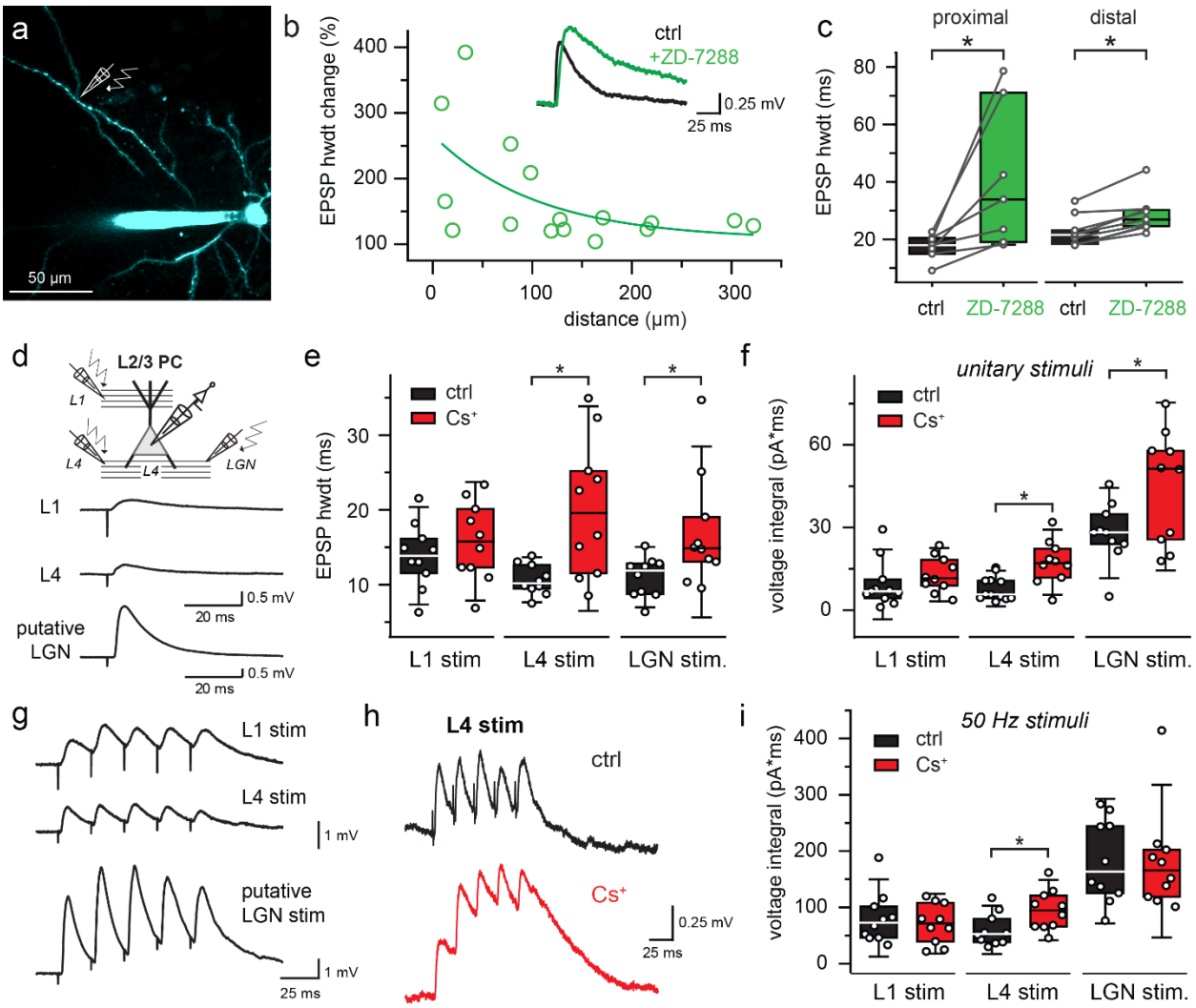

Fig 3. Noncanonical effect of I_h block on EPSP kinetics

a. Experimental arrangement of extracellular targeted stimulation of a L2/3 PC dendrite. **b.** Application of ZD-7288 revealed a proximal bias for EPSP modulation by I_h (Exponential fit τ=104.7 µm, R^2=0.33, n=18). **c.** EPSP halfwidth is significantly modulated along the dendritic axis by I_h, (proximal dendritic locations: 17.42 ± 1.68 ms vs. 40.95 ± 24.78 ms for control vs 50µm ZD-7288 bath application, p=0.03, t(6)=2.84, Student's paired t-test, n=7, distal dendritic locations: 22.68 ± 1.78 ms vs. 28.65 ± 2.17 ms for control vs 50µm ZD-7288 bath application, p=2.1^{-4}, t(8)=-6.39, Student's paired t-test, n=9)**. d.** Schematic illustration of the experimental arrangement. L2/3 PCs were recorded in whole-cell current clamp mode, and a stimulating electrode was placed either in L1 or L4. **e.** I_h modulates EPSP halfwidth for L4 stimulation, but not for L1 (13.87 ± 1.37 ms vs. 15.8 ± 1.67 ms for control vs CsMeSO4 bath application in L1, p=0.38, t(18)=-0.89, Student's two-sample t-test, n=10 each, 10.65 ± 0.64 ms vs.

20.17 ± 2.88 ms for control vs CsMeSO4 bath application in L4, p=0.005, t(18)=-3.22, Student's two-sample t-test, n=10 each, 11.01 ± 0.85 ms vs. 17.05 ± 2.41 ms for control vs CsMeSO4 bath application for putative LGN events, p=0.03, t(18)=-2.36, Student's two-sample t-test, n=10 each). **f.** Pathway-specific I_h effect on unitary EPSP voltage integral (9.35 ± 2.54 pA*ms vs. 12.9 ± 2.04 pA*ms for control vs CsMeSO4 bath application in L1, p=0.3, t(19)=-1.07, Student's two-sample t-test, n=11 and n=10 respectively, 7.85 ± 1.24 pA*ms vs. 17.39 ± 2.5 pA*ms for control vs CsMeSO4 bath application in L4, p=0.002, t(20)=-3.6, Student's two-sample t-test, n=12 and n=10 respectively, 28.01 ± 3.45 pA*ms vs. 44.89 ± 6.42 pA*ms for control vs CsMeSO4 bath application for putative LGN events, p=0.03, t(18)=-2.31, Student's two-sample t-test, n=10 each). **g.** Representative recordings of 50 Hz repeated extracellular stimuli (L1 – grey, L4 – blue, putative LGN -green). **h.** Pathway-specific I_h modulation of synaptic summation (81.05 ± 14.5 pA*ms vs. 71.07 ± 11.19 pA*ms for control vs CsMeSO4 bath application in L1, p=0.6, t(18)=0.54, Student's two-sample t-test, n=10 each, 60.06 ± 9.03 pA*ms vs. 95.15 ± 11.29 pA*ms for control vs CsMeSO4 bath application in L4, p=0.03, t(18)=-2.42, Student's two-sample t-test, n=10 each, 182.08 ± 23.36 pA*ms vs. 182.05 ± 28.59 pA*ms for control vs CsMeSO4 bath application for putative LGN events, p=0.99, t(18)=$8.74*10^{-4}$, Student's two-sample t-test, n=10 each). **i.** Temporal summation of L4 stimulation in control conditions (black) and during CsMeSO4 application (red).

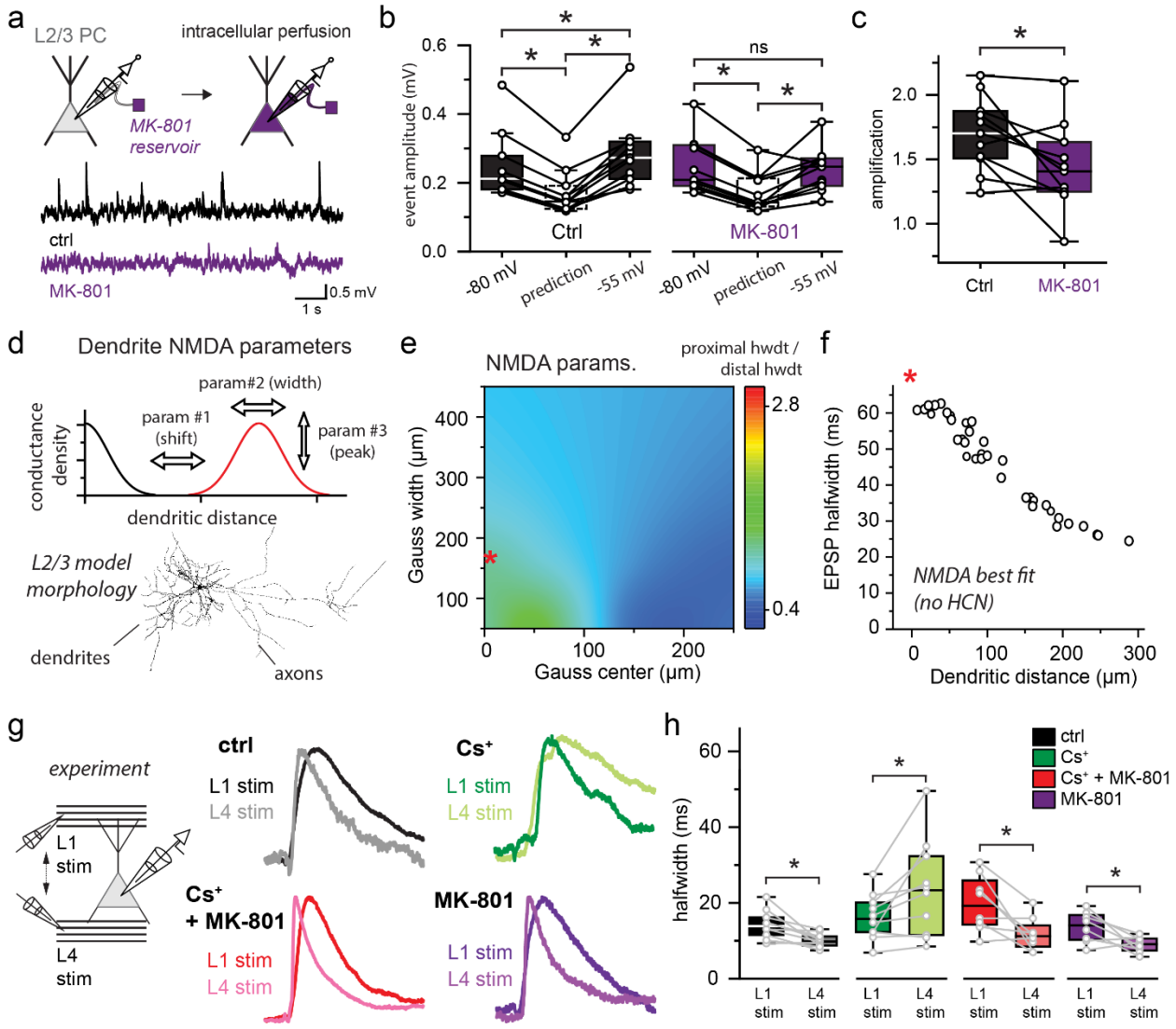

Fig 4. Pathway-specific NMDA receptor boosting of synaptic information

a. Schematic illustration of intracellular pipette solution perfusion during whole-cell patch clamp recordings. Briefly, the pipette was filled with control recording solution (black trace), which was exchanged to an intracellular solution containing 50 µM MK-801 (purple trace) during the recording. **b.** Mean peak amplitude of sEPSPs measured at two different membrane potentials and two different recording conditions (ctrl -80 mV vs. ctrl prediction: $p=4.72*10^{-6}$, t(10) = 8.86, ctrl -80 mV vs ctrl -55 mV: p=0.02, t(10) = -2.81, ctrl prediction vs ctrl -55 mV: $p=1.63*10^{-5}$, t(10) = -7.71, MK-801 -80 mV vs. MK-801 prediction: $p=1.15*10^{-6}$, t(10) = 10.36, MK-801 -80 mV vs MK-801 -55 mV: p=0.58, t(10) = 0.57, MK-801 prediction vs MK-801 -55 mV: $p=2.69*10^{-3}$, t(10) = -3.95, Student's paired-sample t-test, n = 11 for each). **c.** Synaptic amplification estimated by dividing the predicted peak

amplitude from the hyperpolarized recordings and the measured peak at depolarized membrane potentials (1.69 ± 0.09 and 1.43 ± 0.1 for ctrl and MK-801 amplification respectively, p=0.01, t(10) = 3.04, Student's paired-sample t-test, n=11). **d.** Schematic illustration of the multiparameter NEURON fitting procedure for dendritic NMDA. To cover feasible conductance distributions, the localization of channels along the somato-dendritic axis was set by a Gaussian curve, which was shifted in space, in peak and in width as well (top). Simulations were carried out using fully reconstructed L2/3 PC dendrite from the Allen Institute open-source database (bottom). **e.** Inserting NMDA receptors into proximally located simulated synapses recreates experimentally determined distance-halfwidth relationship. **f.** Best fit of the distance-dependent EPSP halfwidth changes (without HCN). Red asterisk denotes the best fit parameter-space on panel **e. g.** Amplitude-normalized EPSPs recorded from L2/3 PCs by minimal stimulation in either in L1 (dark color tones) or L4 (light color tones) in different recording conditions (ctrl: *black*, extracellular cesium: *green*, extracellular cesium + intracellular MK-801: *red*, intracellular MK-801: *purple*). **h.** The broadening effect of cesium is reversed by NMDA receptor block (14.25 ± 1.17 ms and 10.11 ± 0.56 ms for L1 vs L4 stimuli in control conditions, $p=6.73*10^{-3}$, t(9)=3.5, Student's paired-sample t-test, n=10 each, 16.22 ± 1.91 ms and 23.61 ± 4.04 ms for L1 vs L4 stimuli during Cs bath application, p=0.03, t(9)=-2.67, Student's paired-sample t-test, n=10 each, 19.92 ± 2.65 ms and 11.8 ± 1.55 ms for L1 vs L4 stimuli during Cs bath application and MK-801 intracellular application, p=0.02, t(7)=3.01, Student's paired-sample t-test, n=8 each, 13.62 ± 1.43 ms and 8.97 ± 0.72 ms for L1 vs L4 stimuli during MK-801 intracellular application, p=0.025, t(7)=2.84, Student's paired-sample t-test, n=8 each).

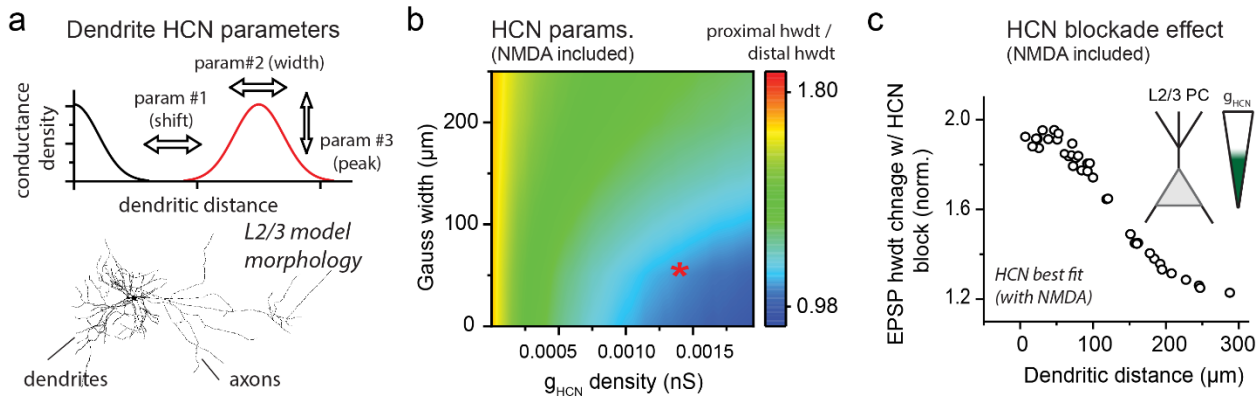

Fig 5. Proximal bias in HCN channel expression dampens NMDA receptor dependent synaptic boosting in a NEURON model simulation.

a. Schematic illustration of the multiparameter NEURON fitting procedure for dendritic HCN, analogous to Fig 4. Simulations included the NMDA dendritic parameters established in Fig. 4. **b**. Proximal abundance of HCN channels recapitulates experimental findings in control conditions. Best fit in the parameter space (denoted with red asterisk) not only recapitulated EPSP halfwidth change, but also our observations regarding changes in input resistance and resting membrane potential. **c.** Schematic illustration of the proposed proximal HCN channel abundance in L2/3 PCs is noted.

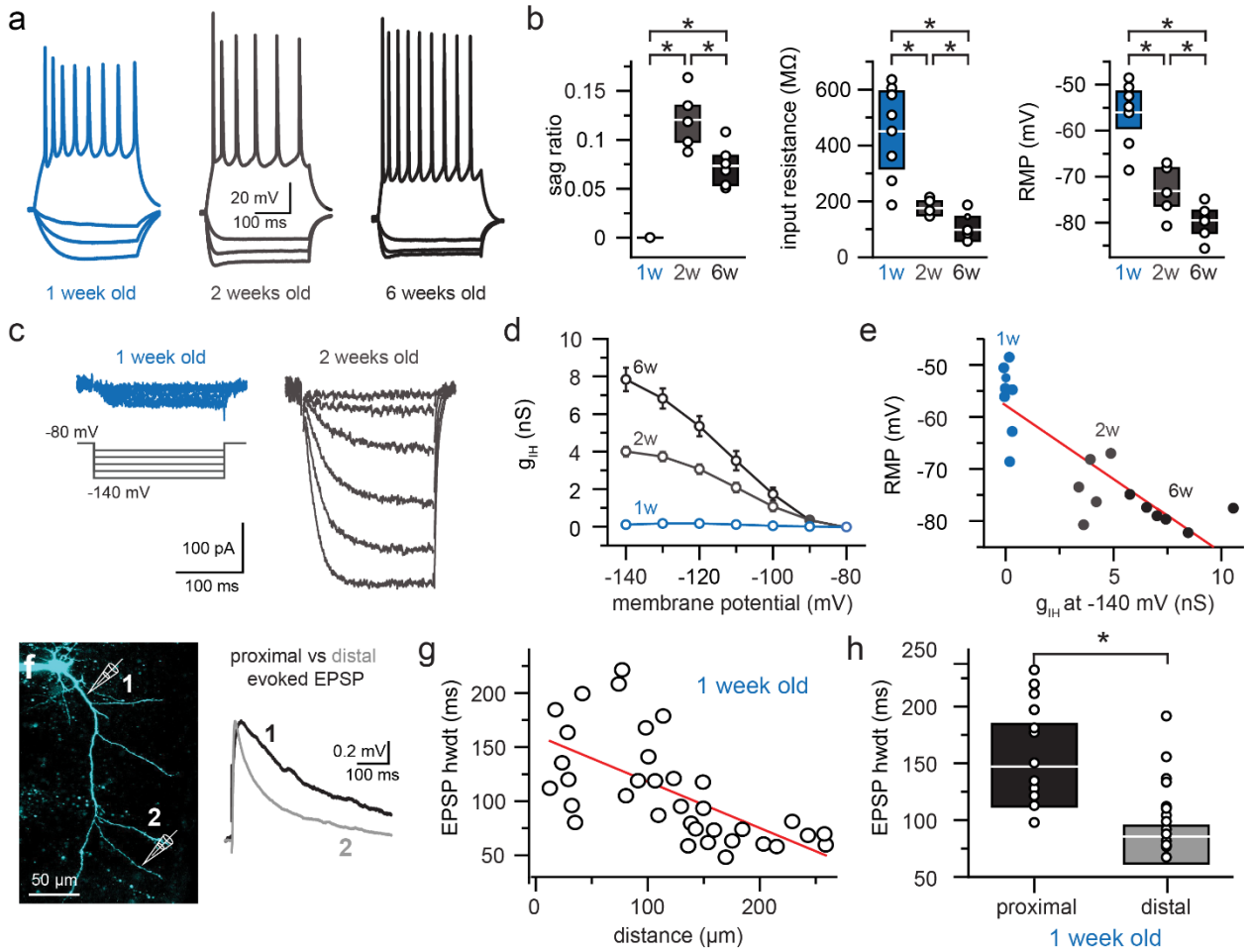

Fig 6. Developmental regulation of I_h expression

a. Representative firing patterns recorded from one week old (left, blue), two weeks old (middle, grey) and six weeks old L2/3 PCs. **b.** Developmental regulation of sag ratio (0.0 ± 0.0, 0.12 ± 0.01 and 0.07 ± 0.01 for one- (n=8), two- (n=5) and six week old L2/3 PCs (n=6), respectively, p=0 for one week old vs two weeks old cells, p=0.01, t(9)=3.04 for two vs six weeks old cells and p=0 for one vs six weeks old cells, Student's two-sample t-test), input resistance (450.6 ± 57.91 MΩ, 175.66 ± 13.66 MΩ and 98.34 ± 18.86 MΩ for one- (n=8), two- (n=5) and six week old L2/3 PCs (n=7), respectively, p=0.004, t(11)=3.65 for one week old vs two weeks old cells, p=0.01, t(10)=3.06 for two vs six weeks old cells and $p=1.11*10^{-4}$, t(13)=5.54 for one vs six weeks old cells, Student's two-sample t-test) and resting membrane potential (-56.05 ± 2.33 mV, -73.13 ± 2.55 mV and -79.47 ± 1.33 MΩ for one- (n=8), two- (n=5) and six week old L2/3 PCs (n=7), respectively, $p=5.9*10^{-4}$, t(11)=4.76 for one week old vs two weeks old cells, p=0.04, t(10)=2.39 for two vs six weeks old cells and $p=1.36*10^{-6}$, t(13)=8.37 for one vs six weeks old cells, Student's two-sample t-test). **c.** Representative voltage clamp recordings of

hyperpolarization activated currents in one week old (left, blue), two weeks old (middle, gray) and six weeks old L2/3 PCs (right, black). **d.** Voltage dependence of hyperpolarization activated currents in one week old (blue), two weeks old (gray) and six weeks old L2/3 PCs (black). **e.** Negative correlation between measured hyperpolarization activated current and resting membrane potential during development (Linear fit (red) slope: -2.84 mV/nS, intercept: -57.67 mV, R^2=0.71, n=20). **f.** Two-photon microscopy image depicting a proximal and a distal extracellular stimulating location positioned closely to an Alexa-594 filled L2/3 PC dendrite (left), and the resulting EPSPs (proximal – black, distal – green). **g.** EPSP halfwidth decreases with dendritic distance (Linear fit (red) slope: -0.42 ms/µm, intercept: 161.01 ms, R^2=0.4, n=35). **h.** EPSPs are significantly slower in proximal, than distal dendritic locations (147.07 ± 12.87 ms and 85.57 ± 6.83 ms for control vs CsMeSO4 bath application for putative LGN events, $p=5.31*10^{-5}$, t(33)=4.64, Student's two-sample t-test, n=13 and 22, respectively).

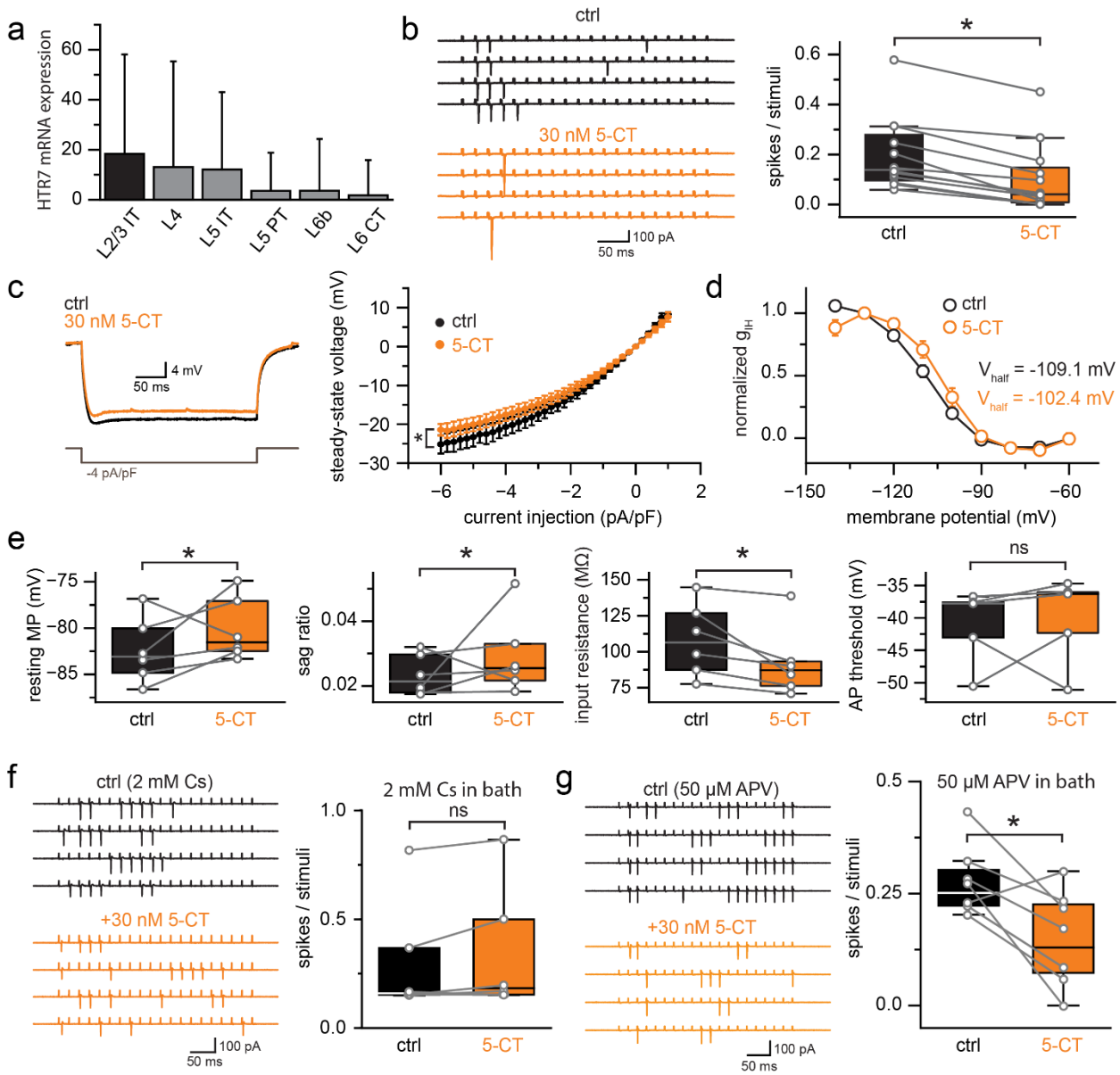

Fig 7. Neuromodulation shifts L2/3 PC excitability via HCN channels

a. $5HT_7$ receptor mRNA is abundantly expressed in L2/3 PCs. Data is collected from the online available dataset(23). **b.** Example cell attached recording of a L2/3 PC (left) upon 50 Hz extracellular stimulation in L4 in control conditions (black) and 5-CT bath application (orange). 5-CT significantly reduced L2/3 PC spiking (0.2 ± 0.04 spike/stimuli vs. 0.1 ± 0.04 spike/stimuli for control vs 5-CT application, $p=3.57*10^{-6}$, t(11)=7.92, Student's paired-sample t-test, n=12 each) **c.** Example current clamp recording of voltage responses to hyperpolarizing current injections (left; control – black, 5-CT – orange). Steady-state voltage response rectification is amplified by $5HT_7R$ blockade (right). **d.** 5-CT shifts the voltage dependence of hyperpolarization activated currents (-109.06 ± 0.47 mV vs -102.35

± 1.09 mV half activation for control vs 5-CT bath application, R^2 = 0.99 for both). **e.** 5-CT did not alter resting membrane potential (-82.41 ± 1.43 mV vs -80.14 ± 1.38 mV in control vs 5-CT bath application, respectively, p=0.89, t(5)=-1.41, Student's paired-sample t-test, n=6 each), sag ratio (0.02 ± $2.55*10^{-3}$ vs 0.03 ± 0.01 in control vs 5-CT bath application, respectively, p=0.82, t(5)=-1.01, Student's paired-sample t-test, n=6 each) and action potential threshold (-41.13 ± 2.6 mV, -40.08 ± 3.05 mV in control vs 5-CT bath application, respectively, p=0.64, t(4)=-0.4, Student's paired-sample t-test, n=5 each), but significantly reduced input resistance (108.21± 10.3 mΩ, 92.29 ± 9.9 MΩ in control vs 5-CT bath application, respectively, p=0.02, t(5)=2.75, Student's paired-sample t-test, n=6 each). **f.** Example recording showing no effect of 5-CT bath application when HCN channels were blocked (left: example recordings, right: 0.3 ± 0.11 spike/stimuli vs 0.34 ± 0.12 spike/stimuli in control vs 5-CT bath application, respectively, p=0.13, t(5)=-1.81, Student's paired-sample t-test, n=6 each). **g.** NMDA independent 5-CT effect on L2/3 PC excitability (0.27 ± 0.03 spike/stimuli vs 0.14 ± 0.04 spike/stimuli in control vs 5-CT bath application, respectively, p=0.01, t(7)=3.66, Student's paired-sample t-test, n=7 each).

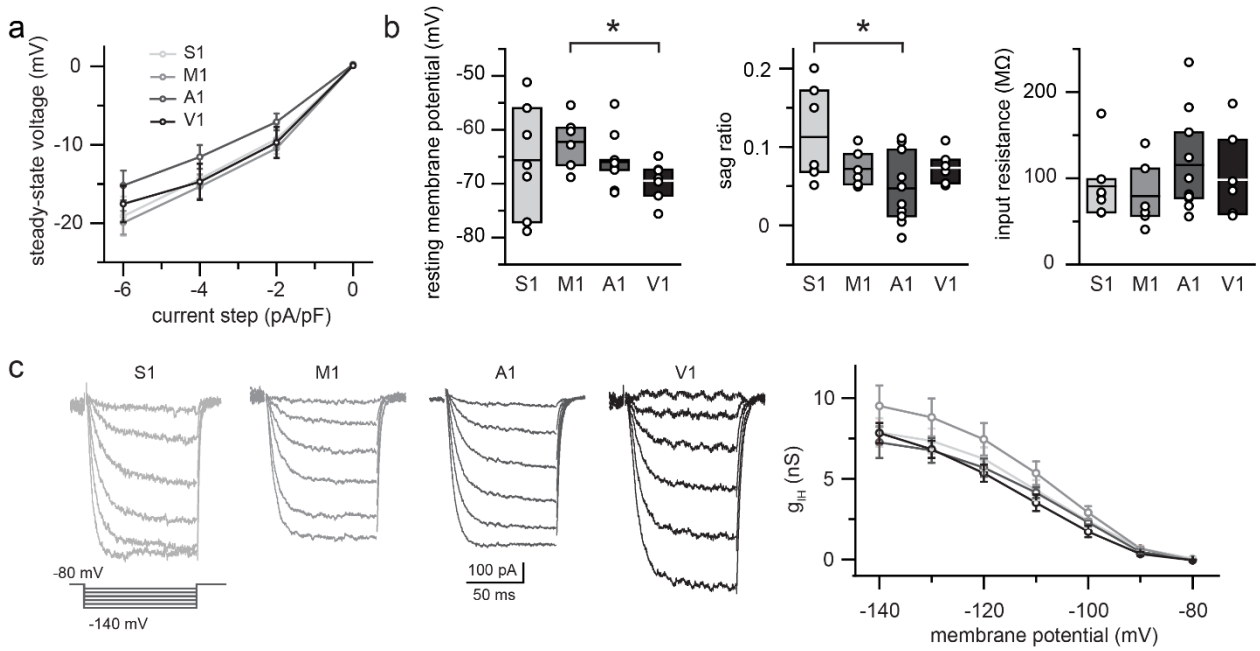

Supplementary Figure 1. Similar Ih current and effect in different cortical areas.

a. Steady-state rectification of L2/3 PCs in the primary somatosensory cortex (S1), primary motor cortex (M1), primary auditory cortex (A1) and primary visual cortex (V1). **b.** Similar resting membrane potential (left), sag ratio (middle) and input resistance (right) of L2/3 PCs in different cortical areas. **c**. Example hyperpolarization activated current recordings from four cortical areas (left), with similar voltage dependent activation (right).

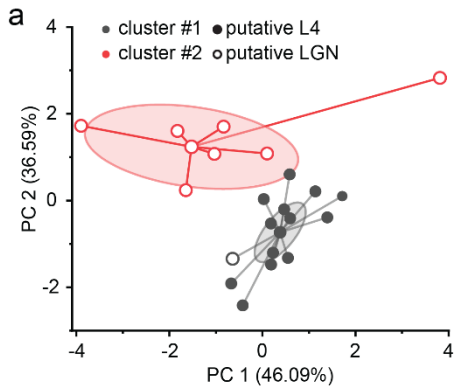

Supplementary Figure 2. Putative LGN and L4 inputs are well separated by k-means clustering

k-means clustering results plotted along the first and second principal component. Ellipses denote the confidence interval; edges are connected to the cluster center. Hollow circles represent putative LGN inputs and filled circles represent L4 inputs determined by the experimenter.

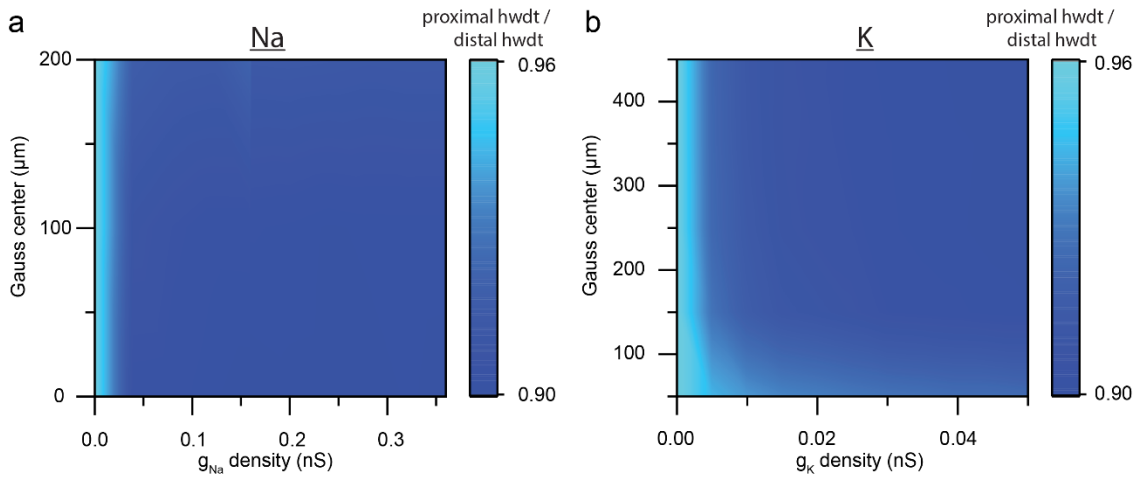

Supplementary Figure 3. The presence of dendritic sodium and potassium channels cannot explain wider proximal synaptic inputs

a. Sodium channels cannot explain the distance-EPSP halfwidth relationship observed when I_h was blocked. Color coding denotes the ratio between proximal and distal EPSP halfwidths. Notice the miniscule range of the color coding. **C.** Same as panel **b.** but for voltage dependent potassium channels.

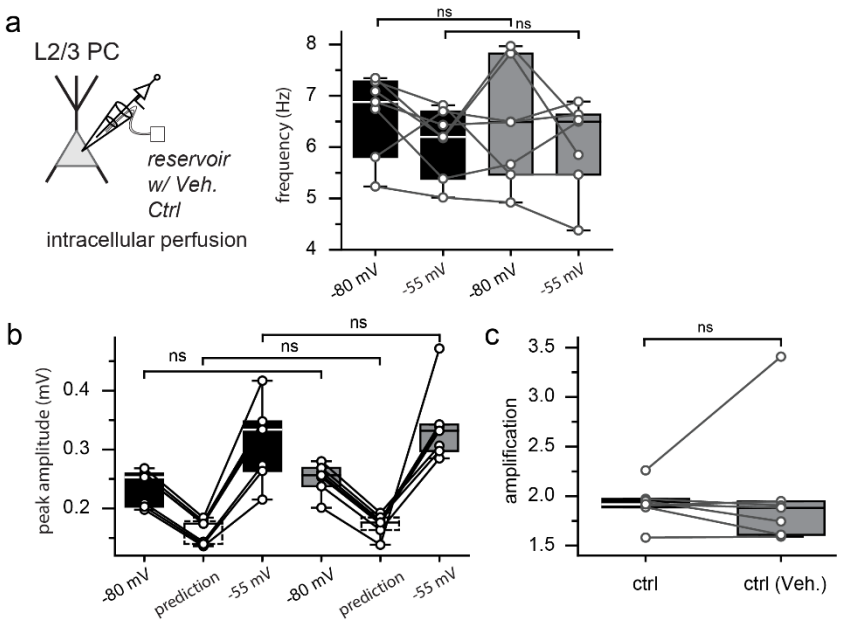

Supplementary Figure 4. Pipette perfusion does not alter spontaneous circuit activity measurements

a. sEPSP frequency is unaltered by pipette perfusion (6.63 ± 0.3 and 6.4 ± 0.44 for ctrl -80 mV and perfused ctrl -80 mV, p=0.57, t(6) = 0.59, 6.1 ± 0.25 and 6.03 ± 0.33 for ctrl -55 mV and perfused ctrl -55 mV, p=0.83, t(6) = 0.23, n=7 for each, Student's paired-sample t-test). **b.** sEPSP peak amplitudes are stable during pipette perfusion experiments (0.23 ± 0.01 and 0.25 ± 0.01 for ctrl -80 mV and perfused ctrl -80 mV, p=0.43, t(6) = -0.83, 0.16 ± 0.01 and 0.17 ± 0.01 for ctrl prediction and perfused prediction, p=0.43, t(6) =-0.83, 0.31 ± 0.03 and 0.34 ± 0.02 for ctrl -55 mV and perfused ctrl -55 mV, p=0.24, t(6) = -1.31, n=7 each, Student's paired-sample t-test). **c.** Pipette perfusion does not alter measured synaptic amplification (1.92 ± 0.07 and 2.01 ± 0.24 for ctrl and perfused ctrl, p=0.65, t(6) = -0.48, n=7 each, Student's paired-sample t-test).

REFERENCES

1. Quiquempoix M, Fayad SL, Boutourlinsky K, Leresche N, Lambert RC, Bessaih T. Layer 2/3 pyramidal neurons control the gain of cortical output. Cell reports. 2018;24(11):2799-807. e4.
2. Wilson DE, Whitney DE, Scholl B, Fitzpatrick D. Orientation selectivity and the functional clustering of synaptic inputs in primary visual cortex. Nature neuroscience. 2016;19(8):1003-9.
3. Hage TA, Bosma-Moody A, Baker CA, Kratz MB, Campagnola L, Jarsky T, et al. Synaptic connectivity to L2/3 of primary visual cortex measured by two-photon optogenetic stimulation. Elife. 2022;11:e71103.
4. Ding Z, Fahey PG, Papadopoulos S, Wang E, Celii B, Papadopoulos C, et al. Functional connectomics reveals general wiring rule in mouse visual cortex. bioRxiv. 2023:2023.03. 13.531369.
5. Scholl B, Wilson DE, Jaepel J, Fitzpatrick D. Functional logic of layer 2/3 inhibitory connectivity in the ferret visual cortex. Neuron. 2019;104(3):451-7. e3.
6. Scholl B, Fitzpatrick D. Cortical synaptic architecture supports flexible sensory computations. Current opinion in neurobiology. 2020;64:41-5.
7. Goetz L, Roth A, Häusser M. Active dendrites enable strong but sparse inputs to determine orientation selectivity. Proceedings of the National Academy of Sciences. 2021;118(30):e2017339118.
8. Smith SL, Smith IT, Branco T, Häusser M. Dendritic spikes enhance stimulus selectivity in cortical neurons in vivo. Nature. 2013;503(7474):115-20.
9. Ujfalussy BB, Makara JK, Lengyel M, Branco T. Global and multiplexed dendritic computations under in vivo-like conditions. Neuron. 2018;100(3):579-92. e5.
10. Landau AT, Park P, Wong-Campos JD, Tian H, Cohen AE, Sabatini BL. Dendritic branch structure compartmentalizes voltage-dependent calcium influx in cortical layer 2/3 pyramidal cells. Elife. 2022;11:e76993.
11. Ferrarese L, Jouhanneau J-S, Remme MW, Kremkow J, Katona G, Rózsa B, et al. Dendrite-specific amplification of weak synaptic input during network activity in vivo. Cell reports. 2018;24(13):3455-65. e5.
12. Luo H, Hasegawa K, Liu M, Song W-J. Comparison of the upper marginal neurons of cortical layer 2 with layer 2/3 pyramidal neurons in mouse temporal cortex. Frontiers in Neuroanatomy. 2017;11:115.
13. Stuart GJ, Spruston N. Dendritic integration: 60 years of progress. Nature neuroscience. 2015;18(12):1713-21.
14. Takahashi N, Oertner TG, Hegemann P, Larkum ME. Active cortical dendrites modulate perception. Science. 2016;354(6319):1587-90.
15. Suzuki M, Larkum ME. General anesthesia decouples cortical pyramidal neurons. Cell. 2020;180(4):666-76. e13.
16. Xu N-l, Harnett MT, Williams SR, Huber D, O'Connor DH, Svoboda K, et al. Nonlinear dendritic integration of sensory and motor input during an active sensing task. Nature. 2012;492(7428):247-51.
17. Shah MM. Cortical HCN channels: function, trafficking and plasticity. The Journal of physiology. 2014;592(13):2711-9.
18. Lörincz A, Notomi T, Tamás G, Shigemoto R, Nusser Z. Polarized and compartment-dependent distribution of HCN1 in pyramidal cell dendrites. Nature neuroscience. 2002;5(11):1185-93.
19. Wahl-Schott C, Biel M. HCN channels: structure, cellular regulation and physiological function. Cellular and molecular life sciences. 2009;66:470-94.
20. Benarroch EE. HCN channels: function and clinical implications. Neurology. 2013;80(3):304-10.
21. Nolan MF, Dudman JT, Dodson PD, Santoro B. HCN1 channels control resting and active integrative properties of stellate cells from layer II of the entorhinal cortex. Journal of Neuroscience. 2007;27(46):12440-51.

824 22. Williams SR, Stuart GJ. Site independence of EPSP time course is mediated by dendritic I h in
825 neocortical pyramidal neurons. Journal of neurophysiology. 2000;83(5):3177-82.
826 23. Gouwens NW, Sorensen SA, Baftizadeh F, Budzillo A, Lee BR, Jarsky T, et al. Integrated
827 morphoelectric and transcriptomic classification of cortical GABAergic cells. Cell. 2020;183(4):935-53. e19.
828 24. Harnett MT, Magee JC, Williams SR. Distribution and function of HCN channels in the apical
829 dendritic tuft of neocortical pyramidal neurons. Journal of Neuroscience. 2015;35(3):1024-37.
830 25. Magee JC. Dendritic Ih normalizes temporal summation in hippocampal CA1 neurons. Nature
831 neuroscience. 1999;2(6):508-14.
832 26. Vetter P, Roth A, Häusser M. Propagation of action potentials in dendrites depends on dendritic
833 morphology. Journal of neurophysiology. 2001;85(2):926-37.
834 27. Malinow R. Transmission between pairs of hippocampal slice neurons: quantal levels, oscillations,
835 and LTP. Science. 1991;252(5006):722-4.
836 28. Yang W, Carrasquillo Y, Hooks BM, Nerbonne JM, Burkhalter A. Distinct balance of excitation and
837 inhibition in an interareal feedforward and feedback circuit of mouse visual cortex. Journal of
838 Neuroscience. 2013;33(44):17373-84.
839 29. Balcioglu A, Gillani R, Doron M, Burnell K, Ku T, Erisir A, et al. Mapping thalamic innervation to
840 individual l2/3 pyramidal neurons and modeling their 'readout'of visual input. Nature Neuroscience.
841 2023;26(3):470-80.
842 30. Sermet BS, Truschow P, Feyerabend M, Mayrhofer JM, Oram TB, Yizhar O, et al. Pathway-, layer-
843 and cell-type-specific thalamic input to mouse barrel cortex. elife. 2019;8:e52665.
844 31. London M, Hausser M. Dendritic computation. Annual review of neuroscience. 2005;28(1):503-
845 32.
846 32. Berger T, Senn W, Lüscher H-R. Hyperpolarization-activated current I h disconnects somatic and
847 dendritic spike initiation zones in layer V pyramidal neurons. Journal of neurophysiology.
848 2003;90(4):2428-37.
849 33. Tsay D, Dudman JT, Siegelbaum SA. HCN1 channels constrain synaptically evoked Ca2+ spikes in
850 distal dendrites of CA1 pyramidal neurons. Neuron. 2007;56(6):1076-89.
851 34. Billeh YN, Cai B, Gratiy SL, Dai K, Iyer R, Gouwens NW, et al. Systematic integration of structural
852 and functional data into multi-scale models of mouse primary visual cortex. Neuron. 2020;106(3):388-
853 403. e18.
854 35. Palmer LM, Shai AS, Reeve JE, Anderson HL, Paulsen O, Larkum ME. NMDA spikes enhance action
855 potential generation during sensory input. Nature neuroscience. 2014;17(3):383-90.
856 36. Branco T, Häusser M. Synaptic integration gradients in single cortical pyramidal cell dendrites.
857 Neuron. 2011;69(5):885-92.
858 37. Bucurenciu I, Kulik A, Schwaller B, Frotscher M, Jonas P. Nanodomain coupling between Ca2+
859 channels and Ca2+ sensors promotes fast and efficient transmitter release at a cortical GABAergic
860 synapse. Neuron. 2008;57(4):536-45.
861 38. Cornford JH, Mercier MS, Leite M, Magloire V, Häusser M, Kullmann DM. Dendritic NMDA
862 receptors in parvalbumin neurons enable strong and stable neuronal assemblies. Elife. 2019;8:e49872.
863 39. Dodt HU, Frick A, Kampe K, Zieglgänsberger W. NMDA and AMPA receptors on neocortical
864 neurons are differentially distributed. European journal of Neuroscience. 1998;10(11):3351-7.
865 40. Guet-McCreight A, Chameh HM, Mahallati S, Wishart M, Tripathy SJ, Valiante TA, et al. Age-
866 dependent increased sag amplitude in human pyramidal neurons dampens baseline cortical activity.
867 Cerebral Cortex. 2023;33(8):4360-73.
868 41. Santello M, Nevian T. Dysfunction of cortical dendritic integration in neuropathic pain reversed
869 by serotoninergic neuromodulation. Neuron. 2015;86(1):233-46.
870 42. Dori I, Dinopoulos A, Blue M, Parnavelas J. Regional differences in the ontogeny of the
871 serotonergic projection to the cerebral cortex. Experimental neurology. 1996;138(1):1-14.

872 43. Vasefi MS, Yang K, Li J, Kruk JS, Heikkila JJ, Jackson MF, et al. Acute 5-HT7 receptor activation
873 increases NMDA-evoked currents and differentially alters NMDA receptor subunit phosphorylation and
874 trafficking in hippocampal neurons. Molecular brain. 2013;6:1-9.
875 44. Megıas M, Emri Z, Freund T, Gulyas A. Total number and distribution of inhibitory and excitatory
876 synapses on hippocampal CA1 pyramidal cells. Neuroscience. 2001;102(3):527-40.
877 45. Nevian T, Larkum ME, Polsky A, Schiller J. Properties of basal dendrites of layer 5 pyramidal
878 neurons: a direct patch-clamp recording study. Nature neuroscience. 2007;10(2):206-14.
879 46. Hubel DH, Wiesel TN. Brain mechanisms of vision. Scientific American. 1979;241(3):150-63.
880 47. Hubel DH, Wiesel TN. Brain and visual perception: the story of a 25-year collaboration: Oxford
881 University Press; 2004.
882 48. Scholl B, Thomas CI, Ryan MA, Kamasawa N, Fitzpatrick D. Cortical response selectivity derives
883 from strength in numbers of synapses. Nature. 2021;590(7844):111-4.
884 49. Waters J, Larkum M, Sakmann B, Helmchen F. Supralinear Ca2+ influx into dendritic tufts of layer
885 2/3 neocortical pyramidal neurons in vitro and in vivo. Journal of Neuroscience. 2003;23(24):8558-67.
886 50. Major G, Polsky A, Denk W, Schiller J, Tank DW. Spatiotemporally graded NMDA spike/plateau
887 potentials in basal dendrites of neocortical pyramidal neurons. Journal of neurophysiology.
888 2008;99(5):2584-601.
889 51. Harris JA, Mihalas S, Hirokawa KE, Whitesell JD, Choi H, Bernard A, et al. Hierarchical organization
890 of cortical and thalamic connectivity. Nature. 2019;575(7781):195-202.
891 52. Rowan MJ, Christie JM. Rapid state-dependent alteration in Kv3 channel availability drives flexible
892 synaptic signaling dependent on somatic subthreshold depolarization. Cell reports. 2017;18(8):2018-29.
893 53. Levelt CN, Hübener M. Critical-period plasticity in the visual cortex. Annual review of
894 neuroscience. 2012;35:309-30.
895 54. Bard JA, Zgombick J, Adham N, Vaysse P, Branchek TA, Weinshank RL. Cloning of a novel human
896 serotonin receptor (5-HT7) positively linked to adenylate cyclase. Journal of Biological Chemistry.
897 1993;268(31):23422-6.
898 55. Karmarkar UR, Dan Y. Experience-dependent plasticity in adult visual cortex. Neuron.
899 2006;52(4):577-85.
900 56. Hensch TK, Bilimoria PM, editors. Re-opening windows: manipulating critical periods for brain
901 development. Cerebrum: the Dana forum on brain science; 2012: Dana Foundation.
902 57. Nolan MF, Malleret G, Dudman JT, Buhl DL, Santoro B, Gibbs E, et al. A behavioral role for dendritic
903 integration: HCN1 channels constrain spatial memory and plasticity at inputs to distal dendrites of CA1
904 pyramidal neurons. Cell. 2004;119(5):719-32.
905 58. Wu J, El-Hassar L, Datta D, Thomas M, Zhang Y, Jenkins DP, et al. Interaction Between HCN and
906 Slack Channels Regulates mPFC Pyramidal Cell Excitability and Working Memory. bioRxiv. 2023:2023.03.
907 04.529157.
908 59. Yu L, Tasaki S, Schneider JA, Arfanakis K, Duong DM, Wingo AP, et al. Cortical proteins associated
909 with cognitive resilience in community-dwelling older persons. JAMA psychiatry. 2020;77(11):1172-80.
910 60. Ramírez D, Zúñiga R, Concha G, Zúñiga L. HCN channels: new therapeutic targets for pain
911 treatment. Molecules. 2018;23(9):2094.
912 61. Ku SM, Han M-H. HCN channel targets for novel antidepressant treatment. Neurotherapeutics.
913 2017;14(3):698-715.
914 62. Kim CS, Johnston D. A possible link between HCN channels and depression. Chronic Stress.
915 2018;2:2470547018787781.
916 63. Postea O, Biel M. Exploring HCN channels as novel drug targets. Nature reviews Drug discovery.
917 2011;10(12):903-14.

64. Lyman KA, Han Y, Chetkovich DM. Animal models suggest the TRIP8b-HCN interaction is a therapeutic target for major depressive disorder. Expert Opinion on Therapeutic Targets. 2017;21(3):235-7.
65. Fukuyama K, Motomura E, Okada M. Therapeutic potential and limitation of serotonin type 7 receptor modulation. International Journal of Molecular Sciences. 2023;24(3):2070.
66. Ishibashi T, Horisawa T, Tokuda K, Ishiyama T, Ogasa M, Tagashira R, et al. Pharmacological profile of lurasidone, a novel antipsychotic agent with potent 5-hydroxytryptamine 7 (5-HT7) and 5-HT1A receptor activity. Journal of Pharmacology and Experimental Therapeutics. 2010;334(1):171-81.
67. Shimizu M, Mi X, Toyoda F, Kojima A, Ding W-G, Fukushima Y, et al. Propofol, an Anesthetic Agent, Inhibits HCN Channels through the Allosteric Modulation of the cAMP-Dependent Gating Mechanism. Biomolecules. 2022;12(4):570.
68. Chen X, Shu S, Kennedy DP, Willcox SC, Bayliss DA. Subunit-specific effects of isoflurane on neuronal I h in HCN1 knockout mice. Journal of neurophysiology. 2009;101(1):129-40.
69. Taylor AL. What we talk about when we talk about capacitance measured with the voltage-clamp step method. Journal of computational neuroscience. 2012;32(1):167-75.
70. Desai NS, Gray R, Johnston D. A dynamic clamp on every rig. eneuro. 2017;4(5).
71. Oláh VJ, Tarcsay G, Brunner J. Small size of recorded neuronal structures confines the accuracy in direct axonal voltage measurements. Eneuro. 2021;8(4).
72. Testa-Silva G, Rosier M, Honnuraiah S, Guzulaitis R, Megias AM, French C, et al. High synaptic threshold for dendritic nmda spike generation in human layer 2/3 pyramidal neurons. Cell reports. 2022;41(11).